Nitrogen-rich conjugated macrocycles: Synthesis, conductivity, and application in electrochemical CO_2 capture

Phuong H. Le,[a] Andong Liu,[b] Leo B. Zasada,[a] Jackson Geary,[a] Ashlyn A. Kamin,[a] Devin S. Rollins,[a] Hao A. Nguyen,[a] Audrey M. Hill,[a] Yayuan Liu,[b] Dianne J. Xiao[a,*]

[a] Department of Chemistry, University of Washington, Seattle, Washington 98195-1700, United States

[b] Department of Chemical and Biomolecular Engineering, Johns Hopkins University, Baltimore, Maryland 21218, United States

* Correspondence to: djxiao@uw.edu

ABSTRACT: Here we report a series of nitrogen-rich conjugated macrocycles that mimic the structure and function of semiconducting 2D metal–organic and covalent organic frameworks while providing greater solution processability and surface tunability. Using a new tetraaminotriphenylene building block that is compatible with both coordination chemistry and dynamic covalent chemistry reactions, we have synthesized two distinct macrocyclic cores containing Ni–N and phenazine-based linkages, respectively. The fully conjugated macrocycle cores support strong interlayer stacking, accessible nanochannels, and out-of-plane charge transport, with pressed pellet conductivities of 10^{-3} S/cm observed for the nickel variants. Finally, using electrochemically mediated CO_2 capture as an example, we illustrate how phenazine macrocycles dramatically improve electrical contact and active site electrochemical accessibility relative to bulk framework powders. Together, these results highlight how simple macrocycles can enable new synthetic directions as well as new applications by combining the properties of crystalline porous frameworks, the processability of nanomaterials, and the precision of molecular synthesis.

Introduction. There has been rising recent interest in downsizing crystalline porous frameworks to the nanoscale, motivated by the inherent processability and mass transport benefits of nanomaterials.[1–3] At the extreme limit of this endeavor is the construction of discrete molecular cages and macrocycles whose structures mimic individual pores found in bulk metal–organic and covalent organic frameworks.[4–8] These nanosized molecules often retain the original function and porosity found in their parent frameworks while introducing new properties. For example, the greater processability of cages and macrocycles facilitates their incorporation into gas separation membranes,[9–11] electronic devices,[12] and modified electrodes for electrocatalysis.[13,14] Depending on the application, the ability to easily deposit thin layers of active material can reduce cost, minimize mass transport losses, and maximize active site utilization. From a fundamental materials discovery standpoint, soluble porous molecules also enable the formation of new composite materials, such as the use of charged metal–organic cages to achieve solid porous salts with tunable compositions.[15] Finally, relative to extended frameworks, porous molecules can also undergo much greater structural changes in response to stimuli, such as the reversible self-assembly and dissolution of aggregated architectures.[16–18]

Our lab has been interested in truncating two-dimensional semiconducting metal–organic frameworks (MOFs) and covalent organic frameworks (COFs) into discrete macrocycles that merge the physical properties of crystalline frameworks with the processability of soft materials.[12] We recently used the ditopic, tetrahydroxy ligand H_4TOTP-OR (H_4TOTP = 2,3,6,7-tetrahydroxytriphenylene) to construct conjugated copper macrocycles that resemble fragments of electrically conductive 2D metal–organic frameworks.[12,19] The macrocycles self-assemble into π-stacked nanotubes that preserve the porosity and out-of-plane charge transport found in the parent framework.

Solution processability is a key property that differentiates macrocycles from bulk 2D framework materials. In the presence of solvent, the noncovalent interactions between macrocycles can be partially broken to achieve short stacks of aggregated macrocycles with good colloidal stability. In certain cases, these noncovalent interactions can even be fully replaced to achieve individual molecules dissolved in solution, though we have found such examples to be rare for metal–organic macrocycles with large extended π-systems.[12] The improved processability provides significant advantages with respect to device fabrication. For example, in our previous work, we showed how fully soluble macrocycles can be leveraged to fabricate thin-film field-effect transistor devices.[12]

In this work, we expand upon our previous studies by introducing a new ditopic triphenylene-based ligand containing nitrogen bridging atoms (**Fig. 1**). Using this ligand, we illustrate both the broad generalizability of our synthetic approach as well as the beneficial impact of framework truncation on electrochemical performance. On the synthetic front, the presence of nitrogen donors dramatically expands the potential diversity of macrocycle structures. The greater nucleophilicity of nitrogen compared to oxygen provides access to a wider range of bond-forming reactions. For example, *o*-phenylenediamine units can react with 1,2-diketones, aldehydes, and *ortho*-difluorinated aromatic compounds to form phenazine,[20–24] imidazole,[25,26] and piperazine[27,28] linkages, respectively (**Fig. 1a**). In the context of

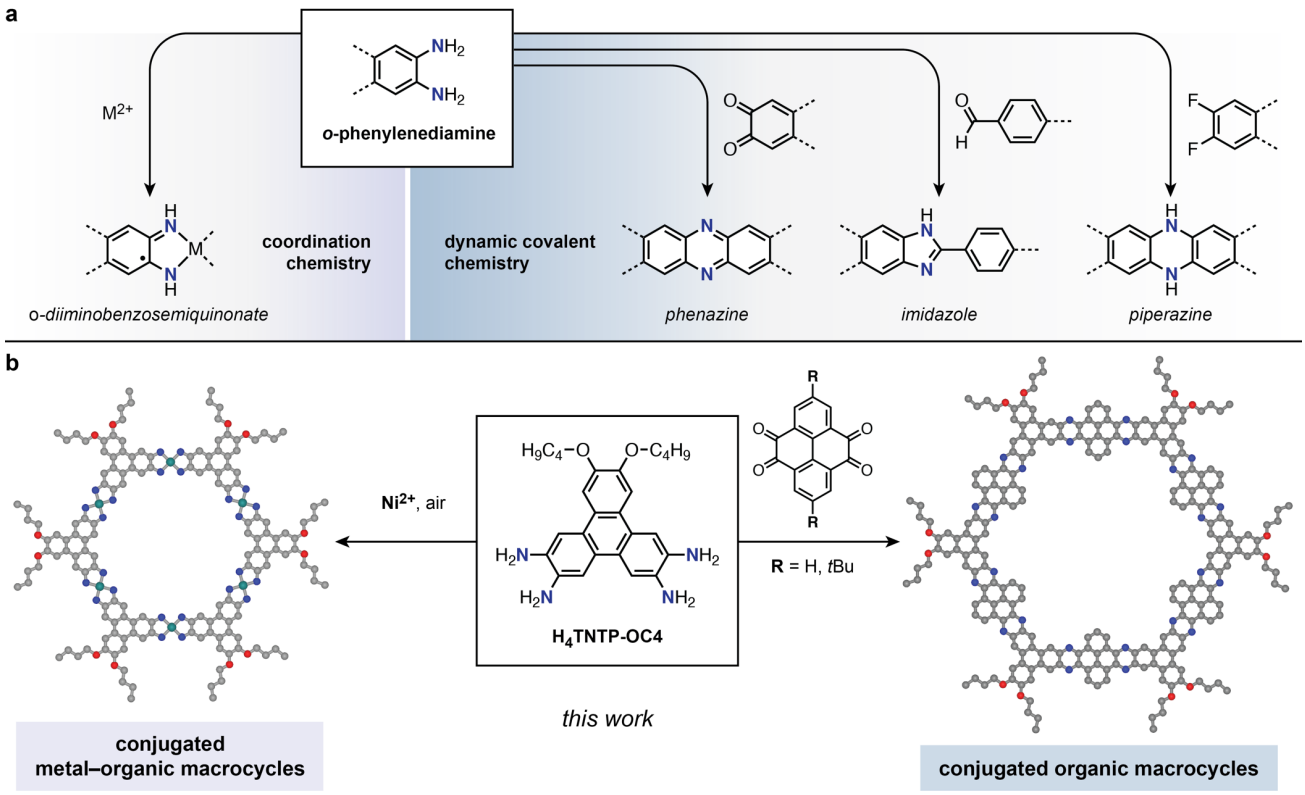

Fig. 1 | (a) Schematic illustration of the different linkages that can be formed from *o*-phenylenediamine precursors via coordination chemistry and dynamic covalent chemistry. (b) Construction of metal–organic macrocycles and conjugated organic macrocycles starting from the bis(alkoxy)-tetraaminotriphenylene ligand, H_4TNTP-OC4.

metal–organic materials, nitrogen donors also provide superior charge transport properties relative to oxygenated analogues due to increased metal–ligand covalency.[29,30]

On the application front, we hypothesized that framework truncation should also improve electrochemical device performance. Colloidal nanoparticles composed of aggregated π-stacked metal–organic macrocycles expose significantly greater external surface area relative to bulk micron-scale framework powders. In principle, this increased external surface area should reduce both mass transport and charge transport limitations.

Here we show that the ditopic ligand H_4TNTP-OC4 (H_4TNTP-OC4 = 10,11-dibutoxytriphenylene-2,3,6,7-tetraamine) can be used to construct nitrogen-rich conjugated metal–organic and organic macrocycles that resemble semiconducting 2D MOFs and COFs in both form and function (**Fig. 1b**). Combining H_4TNTP-OC4 and nickel(II) salts produces semiconducting nickel macrocycles with pellet conductivities of 5(1) $\times 10^{-3}$ S/cm. Similarly, reacting H_4TNTP-OC4 with tetraketones forms phenazine-linked conjugated organic macrocycles, which are structurally confirmed by powder X-ray diffraction and solid-state ^{13}C NMR. Finally, we show that phenazine-based macrocycles greatly outperform the analogous 2D COFs as solid sorbents for electrochemically mediated CO_2 capture due to their greater processability and nanoscale dimensions.

Ligand design. We envisioned that bis(alkoxy)-tetraaminotriphenylene ligands could be synthesized following a similar route as the one developed by Northrop and coworkers for bis(alkoxy)-tetrahydroxytriphenylenes.[31] Their approach relies on Suzuki coupling to synthesize *ortho*-terphenyl precursors containing *tert*-butyldimethylsilyl (TBDMS)-protected catechols, which are subsequently oxidatively cyclized and deprotected. We hypothesized that simply replacing the TBDMS-protected catechols with tert-butoxycarbonyl (BOC)-protected *o*-phenylenediamine coupling partners would generate the desired nitrogen-based ligands (**Fig. 2**). Gratifyingly, the proposed synthetic route proceeded smoothly. The desired bis(butoxy)-tetraaminotriphenylene ligand was isolated as the protonated hydrochloride salt (H_4TNTP-OC4·4HCl) in

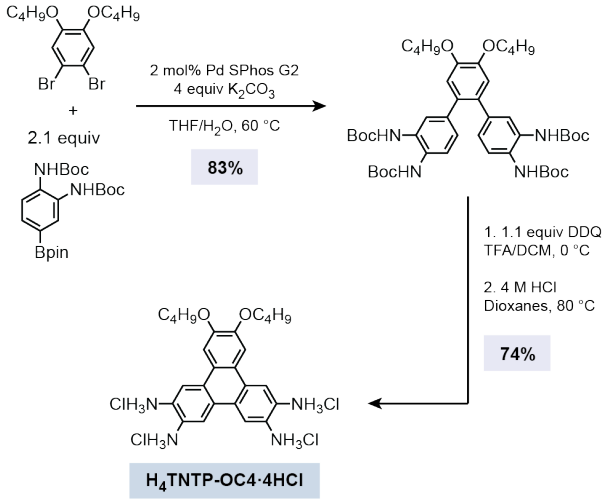

Fig. 2 | Synthesis of the H_4TNTP-OC4 ligand via Suzuki coupling followed by DDQ catalyzed ring closure and BOC protecting group removal.

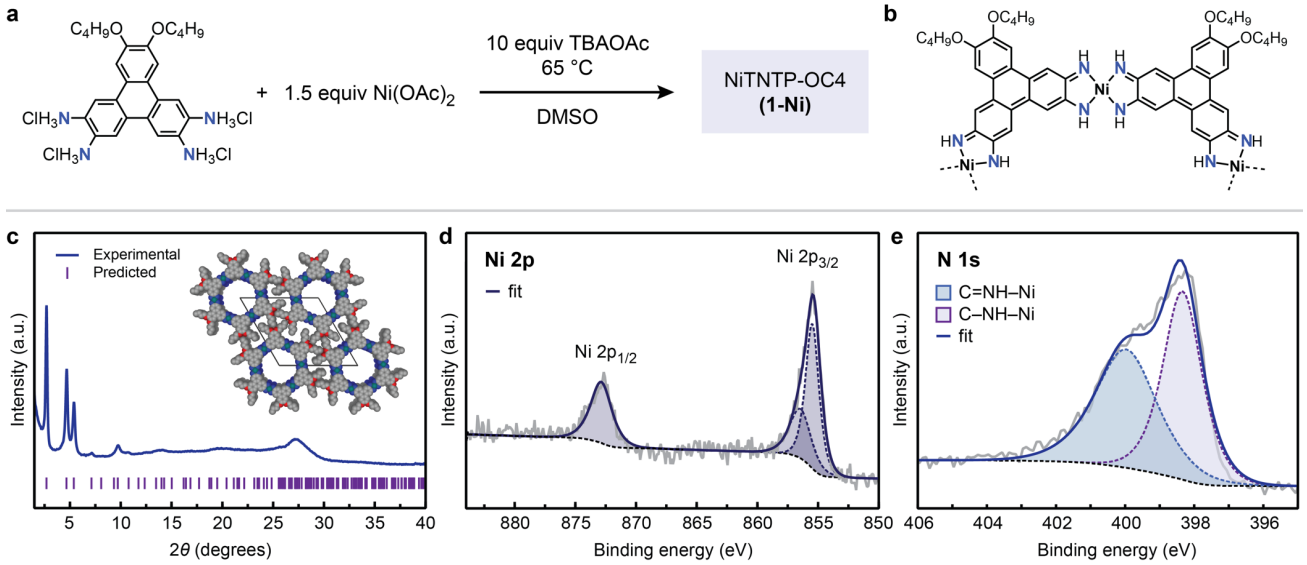

Fig. 3 | (a) Synthesis of **1-Ni**. (b) Proposed structure of **1-Ni**, highlighting the partially oxidized ligand. (c) Experimental powder X-ray diffraction pattern of **1-Ni** along with modeled structure and predicted diffraction peaks. (d) High resolution Ni 2p XPS spectrum, showing the absence of satellite features. (e) High resolution N 1s XPS spectrum, showing the presence of two distinct nitrogen environments.

61% overall yield over three steps (**Fig. 2**). We note that the H_4TNTP-OC4 ligand is always isolated and handled in its protonated form (H_4TNTP-OC4·4HCl) to minimize oxidative degradation. While this work focuses on ligands containing *n*-butyl side chains, the modular synthetic route should allow the peripheral side chains to be readily tuned in future studies.

Synthesis and characterization of nickel macrocycles. Dincă and coworkers reported the first nitrogen-based conjugated 2D metal–organic framework $Ni_3(HITP)_2$ (HITP = 2,3,6,7,10,11-hexaiminotriphenylene) in 2014,[30] with a subsequent follow-up study on mixed-metal variants in 2020.[32] Recent single crystal measurements have shown that the out-of-plane conductivity in $Ni_3(HITP)_2$ is ~100-fold higher than similar 2D frameworks containing oxygen-based ligands, such as $Cu_3(HHTP)_2$.[29,33,34] Given the rich chemistry observed in this particular member of the conjugated 2D MOF family, we were excited to explore the properties of its macrocyclic form.

While the addition of external bases such as alkali acetate salts is critical to the synthesis of $M_3(HITP)_2$ materials,[30,32] we found that the crystallinity of our materials decreased with increasing equivalents of MOAc ($M^+ = Na^+$, K^+). Although moderately crystalline material was obtained using 10 equiv of MOAc (**Fig. S2**), further increasing to 100 equiv led to amorphous powders (**Fig. S3**). We hypothesized that this was due to the unusual solubility characteristics of our ligand, which contains highly polar ammonium groups as well as hydrophobic alkyl chains. Because of the alkyl chains, the small amounts of water required to dissolve the MOAc salt led to rapid precipitation of poorly crystalline product.

We found that two important reaction conditions were necessary to obtain highly crystalline macrocycle. First, we switched to tetrabutylammonium acetate (TBAOAc) as our acetate source. The tetrabutylammonium cation has much greater solubility in organic solvents, allowing us to avoid the use of aqueous solutions. Second, we found that dimethyl sulfoxide (DMSO) was a uniquely enabling solvent for this reaction. No precipitate was formed when *N,N*-dimethylacetamide (DMA) was used, and an amorphous solid was obtained in *N,N*-dimethylformamide (DMF). We note that omitting the acetate was also not acceptable; no precipitate formed in the absence of external base even after a reaction time of one month.

Gratifyingly, heating 1 equiv H_4TNTP-OC4·4HCl, 1.5 equiv $Ni(OAc)_2$, and 10 equiv of TBAOAc in DMSO at 65 °C for 24 h produced the macrocycle NiTNTP-OC4 (**1-Ni**) as a highly crystalline dark blue-black powder with the expected diffraction pattern (**Fig. 3**). Specifically, the first three peaks at 2θ = 2.70, 4.68, and 5.40° follow the 1:1/√3:1/2 ratio in d-spacing expected for a hexagonal unit cell (**Fig. 3c**). Furthermore, based on the position of the first peak, an approximate *a* and *b* dimension of 37.8 Å was obtained. This value is nearly identical to the dimensions of a fully relaxed, geometry optimized model of **1-Ni** ($a = b = 37.92$ Å). Finally, a broad peak centered at 27.1° is observed, which we have assigned as the π–π stacking feature. This peak corresponds to a short distance of ~3.3 Å, which is consistent with both the π–π stacking metrics found in the parent framework $Ni_3(HITP)_2$ (~3.3 Å)[33] as well as our previously reported copper-based metal–organic macrocycles (~3.2 Å).[12]

High-resolution X-ray photoelectron spectroscopy (XPS) measurements were carried out to further probe the chemical environment of our macrocycles and support our structural assignment. Analysis of the Ni 2p spectrum shows a binding energy of ~855 eV for the Ni $2p_{3/2}$ peak and ~873 eV for the $2p_{1/2}$ peak, consistent with a Ni(II) oxidation state (**Fig. 3d**).[35] Importantly, very faint satellite features are observed, as expected for diamagnetic, square planar Ni(II) sites.[35] We note that the presence of weak satellite features associated with paramagnetic Ni(II) sites (e.g., octahedral coordination) is likely due to solvent binding at surface sites or other defects, as similar features are also observed in nanocrystalline $Ni_3(HITP)_2$.[32,36]

In the extended framework $Ni_3(HITP)_2$, it is proposed that each of the three *o*-phenylenediamine units is doubly deprotonated and oxidized by 1 e^- to generate monoanionic, *o*-diiminobenzosemiquinonate sites (**Fig. 1a**). Because our ligand only has two *o*-phenylenediamine units, we propose that a diamagnetic, partially oxidized ligand containing distinct imine and

amine units is formed rather than a diradical species (**Fig. 3b**). This assignment is supported by our N 1s XPS data (**Fig. 3e**). The spectrum can be fit well with two distinct peaks of equal area, one at ~400 eV and a second at ~398 eV. We assign the peak at ~400 eV to the oxidized imine group (C=NH–M), and the lower energy peak to unoxidized amine (C–NH–M).[37]

Interestingly, the structure of **1-Ni** is considerably less sensitive to solvation state than related triphenylene-based macrocycles, such as our previously reported CuTOTP-OR macrocycles[12] and Dichtel and coworkers' boronate ester-linked macrocycles.[38] Minimal changes to the unit cell dimensions (<5%) and peak broadness (5% decrease in FWHM) are observed upon soaking **1-Ni** in DMA and drying the material under vacuum (**Fig. S5** and **Table S2**). In contrast, the diffraction pattern of CuTOTP-OC4 broadens significantly upon drying (28% increase in FWHM), while the *a* and *b* unit cell dimensions of boronate ester-linked macrocycles contract by nearly 10 Å upon desolvation (~18% decrease).[38]

The less dynamic structure of **1-Ni** suggests the material may have more robust interlayer and intercolumn interactions, which should promote porosity and electrical conductivity. Indeed, gas sorption measurements show that the interior channels remain accessible to guest molecules after desolvation. A BET surface area of 130 m^2/g was obtained from 273 K CO_2 adsorption isotherms. We note that a lower surface area of 20 m^2/g was obtained using N_2 at 77 K as a probe molecule. We hypothesize that this reduction in surface area is due to partial pore blockage by frozen butoxy side-chains. Density functional theory (DFT) calculations of the pore size distribution, derived from 77 K N_2 adsorption data, show a single narrow peak at 20 Å (**Fig. S9**), which corresponds with both the crystalline structure of **1-Ni** and the reported pore size of $Ni_3(HITP)_2$.[39]

Excitingly, pressed pellet conductivity measurements provided an average conductivity of $5(1) \times 10^{-3}$ S/cm, which is an order of magnitude higher than our previously reported CuTOTP-OC4 macrocycle ($6(2) \times 10^{-4}$ S/cm). This increase is consistent with previously reported single crystal conductivity measurements on the analogous metal–organic frameworks, which show that the conductivity of $Ni_3(HITP)_2$ rods (~150 S/cm) is approximately two orders of magnitude higher than $Cu_3(HHTP)_2$ rods (~1.5 S/cm).[33]

Together, these results show that metal–organic macrocycles, like the MOFs that inspired their synthesis, are highly tunable. The use of alternative metals and bridging atoms can be leveraged to achieve new families of materials with similar structures but improved charged transport properties. Finally, we note that the macrocycle periphery can also be tailored towards a specific function. For example, while **1-Ni** shows poor colloidal stability in its current form (**Table S5** and **Fig. S12**), side-chain engineering should greatly improve the processability of these materials. Analogous *n*-butyl-functionalized copper macrocycles were shown to be similarly prone to aggregation but could be rendered fully soluble in organic solvents with the addition of longer C18 alkyl chains.[12]

Synthesis and characterization of phenazine-based macrocycles. After successfully synthesizing metal–organic macrocycles using H_4TNTP-OC4, we hypothesized that the same ligand could also be used to form truncated analogues of covalent organic frameworks. As a proof-of-concept, we targeted the synthesis of phenazine-linked macrocycles, as their COF counterparts have become an important and widely studied class of semiconducting crystalline frameworks.[20–24]

While some syntheses of phenazine-linked COFs employ basic conditions,[24] the vast majority use acidic modulators such as acetic acid and sulfuric acid. Heating H_4TNTP-OC4·4HCl (1.2 equiv) and pyrene-4,5,9,10-tetraone (1 equiv) in 1:1 acetic acid/DMF at 120 °C under an N_2 atmosphere produced the macrocycle PyrTNTP-OC4 (**2-Pyr**) as a brown crystalline solid

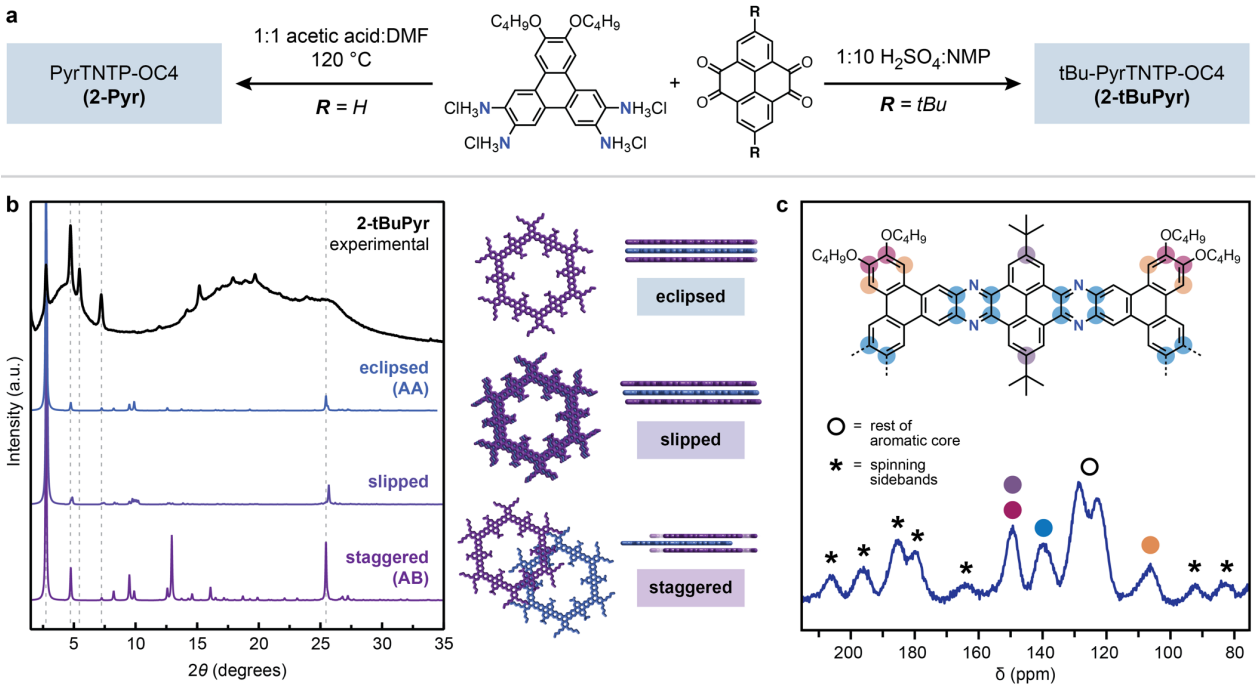

Fig. 4 | (a) Synthesis of two phenazine-based conjugated macrocycles, **2-Pyr** and **2-tBuPyr**. (b) Experimental powder X-ray diffraction pattern alongside predicted diffraction patterns for **2-tBuPyr** with eclipsed, slipped, and staggered π–π stacking motifs. (c) Solid-state ^{13}C NMR spectrum of **2-tBuPyr**. Asterisks denote the spinning sidebands.

(**Fig. 4a** and **Fig. S13**). Overall, the observed experimental powder X-ray diffraction pattern is broadly consistent with structural models optimized in a hexagonal packing arrangement (**Fig. S13**). The first peak is located at $2\theta = 2.36°$, indicating a large *a* and *b* unit cell dimension of 43.2 Å, as expected for a large organic macrocycle with >2 nm pore windows. Furthermore, an intense peak is observed at 26.7°, which we have assigned as the π–π stacking feature. This peak corresponds to a distance of 3.3 Å, which is comparable to the ~3.3–3.5 Å range of π–π stacking distances observed in other planar phenazine-linked COFs.[21–24]

Excitingly, the synthesis could be extended to the di-*tert*-butyl functionalized pyrene-4,5,9,10-tetraone coupling partner as well. Combining H_4TNTP-OC4·4HCl (1.5 equiv) and 2,7-di-*tert*-butylpyrene-4,5,9,10-tetraone (1 equiv) in 1:10 H_2SO_4/*N*-methyl-2-pyrolidone (NMP) at 150 °C under an N_2 atmosphere produced tBu-PyrTNTP-OC4 (**2-tBuPyr**) as a dark reddish brown crystalline solid (**Fig. 4**). The first four diffraction peaks are located at $2\theta = 2.74$, 4.72, 5.44, and 7.22°, consistent with the expected 1:1/√3:1/2:1/√7 ratio in *d*-spacing for a hexagonal unit cell (**Fig. 4b**). A weak, broad peak around $2\theta \sim 25–26°$ is observed, corresponding to a π–π stacking distance of ~3.5 Å. This is slightly larger than the ~3.3 Å observed in **2-Pyr**, which is expected given the bulkier *tert*-butyl substituents. The π–π stacking distance was further confirmed by transmission electron microscopy (TEM), which showed an average distance of 3.46(12) Å between stacked macrocycles (**Fig. S14** and **Table S6**).

Due to the relatively broad diffraction peaks, the exact π–π stacking arrangements adopted by **2-Pyr** and **2-tBuPyr** are difficult to determine with absolute certainty. However, based on modeling studies, we expect the second peak in the diffraction pattern (specifically, the (110) peak) to increase in intensity as the structure deviates further from fully eclipsed (**Fig. S15–17**). Given the strong (110) peak in the experimental diffraction pattern and the presence of sterically bulky *tert*-butyl groups, we hypothesize that **2-tBuPyr** likely adopts either a quasi-AB or AB stacking pattern, with a significant offset between neighboring layers of macrocycles (**Fig. 4b**).[40,41]

The successful formation of phenazine linkages was confirmed spectroscopically through a combination of infrared spectroscopy and solid-state ^{13}C NMR (**Fig. 4c**). The infrared spectrum of **2-tBuPyr** shows the disappearance of the amine N–H stretches and the preservation of the alkyl C–H features, confirming that the H_4TNTP-OC4 backbone is present but the free amine groups have reacted (**Fig. S19**). A small C=O stretching feature at 1660 cm^{-1} is observed, which cannot be removed even after repeating rinsing with solvents such as DMF, methanol (MeOH), and dichloromethane (DCM). We attribute this feature to a small number of unreacted, dangling carbonyl groups resulting from incomplete macrocyclization. Similar residual C=O stretches have been observed in related phenazine-based COFs.[24] We note that the residual C=O stretch is more intense in **2-Pyr**, likely due to the poor solubility of the pyrene-4,5,9,10-tetraone starting material (**Fig. S20**).

While the phenazine ring system is known to display characteristic stretches between 1200–1500 cm^{-1},[20,22,23] these bands were difficult to definitively assign due to the large number of peaks in this region. Vibrational frequency calculations using density functional theory show that this region of the spectra is populated by a large number of skeletal vibrations involving the entirety of the macrocycle core (see **Fig. S21** and the SI for more details). Therefore, we turned to solid-state ^{13}C NMR to confirm the presence of phenazine linkages, as phenazine moieties have a diagnostic peak at ~140 ppm.[20,23,24] Gratifyingly, a new peak at 139.8 ppm is observed in the solid-state ^{13}C NMR spectrum of both **2-Pyr** and **2-tBuPyr** that is not present in the starting ligand (**Fig. 4c and Fig. S23–24)**, confirming the formation of the phenazine unit. While no evidence of dangling carbonyls could be detected in the ^{13}C NMR of **2-tBuPyr**, a small residual carbonyl peak is observed at 172.8 ppm in **2-Pyr** (**Fig. 4c** and **Fig. S23**).

Surface area measurements using CO_2 at 273 K indicate that **2-tBuPyr** has accessible porosity with a BET surface area of 134 m^2/g. Preliminary pressed pellet conductivity measurements show that **2-tBuPyr** has a modest electrical conductivity of $8(1) \times 10^{-10}$ S/cm. This is consistent with previously reported conjugated 2D COFs, which generally display relatively low pellet conductivities of 10^{-10} to 10^{-5} S/cm prior to chemical doping.[42,43]

Finally, we tested the dispersibility of **2-tBuPyr** in organic solvents. Out of the five solvents tested (DMF, DCM, MeOH, tetrahydrofuran, and toluene), **2-tBuPyr** formed the most stable colloidal dispersions in DCM (**Fig. S25** and **Fig. S27**). Dynamic light scattering (DLS) measurements immediately following probe sonication showed that over 90% of the particles were less than 100 nm in diameter, with a smaller population of ~500 nm particles (**Table S7**). This particle size distribution remained relatively constant over the course of 24 hours. However, the population of larger ~400–500 nm particles gradually increases over the period of two weeks, indicating slow aggregation over time. We note that isolating the material via centrifugation, and not filtration, was important to maintaining good dispersibility.

The relative ease by which **2-tBuPyr** can be dispersed in organic solvents highlights the processability advantages of discrete macrocycles over structurally similar extended 2D frameworks. For comparison, we synthesized the analogous 2D COF from 2,3,6,7,10,11-hexaaminotriphenylene (HATP) and 2,7-di-*tert*-butylpyrene-4,5,9,10-tetraone, using a slight modification of the previously reported conditions by Jiang and coworkers.[20] The structure and porosity of the framework, named **CS-COF** in the original report, were confirmed by PXRD and gas adsorption (**Fig. S31–32** and **Table S12**). DLS measurements of the framework, performed immediately after probe sonication in DCM, show a very broad particle distribution centered ~650 nm in diameter (**Fig. S33**). Furthermore, unlike the macrocycle **2-tBuPyr**, the phenazine COF particles rapidly aggregated and settled within the first hour. While colloidally stable imine- and boronate ester-based COF nanoparticles have been reported,[44–46] to our knowledge similar syntheses have not been developed for phenazine-based COFs. This may be due to their exceptionally strong π–π stacking and relatively harsh synthesis conditions.

Electrochemically mediated CO_2 capture. Relative to poorly processable and aggregated COF powders, we hypothesized that the nanoscale dimensions of **2-tBuPyr** may enable improved mass and charge transport and higher performance in electrochemical devices. We anticipated that maximizing electrical contact would be particularly important, as both our organic macrocycles and previously reported 2D COFs have relatively low electrical conductivities (~10^{-10} S/cm, see **Table S9** and **S13**).[42,43]

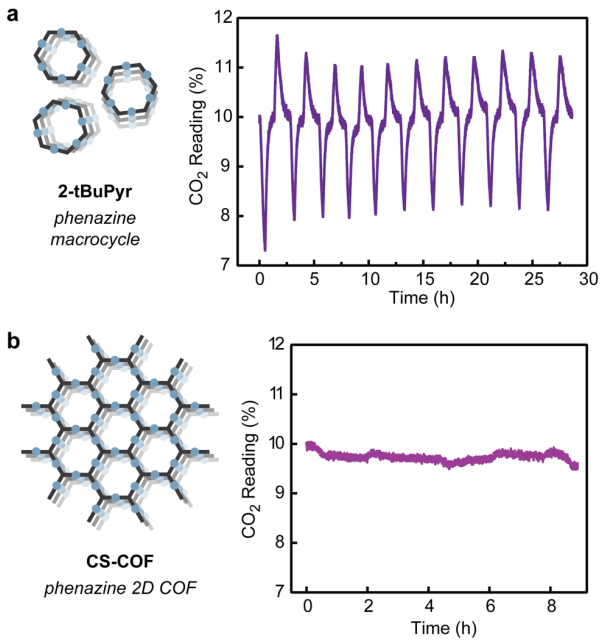

Fig. 5 | Performance of (a) **2-tBuPyr** and (b) the analogous phenazine 2D COF as solid sorbents in a fixed-bed electrochemically mediated CO_2 capture device. The macrocycle **2-tBuPyr** runs for stably for 11 repeated capture and release cycles whereas the 2D COF shows negligible CO_2 uptake under the same conditions.

We identified electrochemically mediated CO_2 capture as an intriguing testing ground for comparing the performance of phenazine-based macrocycles versus 2D covalent organic frameworks. Recent work has shown that the Lewis basicity and CO_2 affinity of phenazine and its derivatives are redox-tunable, allowing these molecules to be used as liquid sorbents for electrochemically mediated carbon capture (EMCC).[47–49] Such molecules form strong adducts with CO_2 upon electrochemical reduction, and readily release the captured CO_2 upon oxidation. We hypothesized that phenazine-based macrocycles and COFs could be used as solid-phase sorbents for EMCC, as the nanochannels should facilitate electrolyte and CO_2 transport.[50]

To validate this assumption, we first collected cyclic voltammograms (CV) of the macrocycle **2-tBuPyr** in the absence and presence of CO_2 (**Fig. S34**). Under an inert N_2 atmosphere, the macrocycle displays a reversible redox pair corresponding to the reduction and oxidation of the sp^2-nitrogen centers in the phenazine moiety, whose half-wave potential ($E_{1/2}$) is –1.63 V versus ferrocenium/ferrocene (Fc^+/Fc). Excitingly, the CV under CO_2 shows a clear anodic shift of the reduction peak, consistent with the formation of a CO_2 adduct that decreases electron density on the reduced macrocycle. Furthermore, the oxidation peak also anodically shifts and becomes electrochemically irreversible, consistent with the presence of a CO_2 adduct whose nitrogen–carbon bond requires extra energy to break upon oxidation.

Next, infrared spectroscopy measurements were carried out to further confirm the formation of stable CO_2 adducts. Excitingly, in the presence of CO_2, a clear peak at ~1715 cm^{-1} emerges after the reduction of **2-tBuPyr**, consistent with carbamate formation (**Fig. S35**).[51]

Encouraged by the CV and IR data, we next constructed a fixed-bed EMCC device to evaluate the performance of the sorbent electrodes under specific CO_2 gas feed conditions. The electrodes were fabricated using an ink of **2-tBuPyr**, Vulcan carbon, and polyvinylidene fluoride (PVDF) binder in a 4:2:1 mass ratio. The performance of our macrocycle sorbent in a cyclic carbon capture and release process is shown in **Fig. 5a**. Using a 10% CO_2 (balanced with N_2) feed stream at a flow rate of 0.4 standard cm^3 min^{-1} (sccm), the fixed bed can run stably for more than 11 cycles (30 hours) with negligible performance decay (see SI for more details).

The three key metrics commonly used for evaluating EMCC performance are summarized in **Fig. 6**. To evaluate the reversibility of **2-tBuPyr**, we define the ratio of the total amount of CO_2 released and captured in each cycle as the release/capture efficiency, and the ratio of the electrochemical oxidation and reduction capacities as the Coulombic efficiency. These two values are averaged to be 76.3% and 84.6%, respectively, illustrating acceptable reversibility (**Fig. 6b**).

The third relevant metric is the CO_2 capacity utilization, or the number of CO_2 molecules captured per transferred electron. The **2-tBuPyr** device shows an average CO_2 capacity utilization of 0.45 equiv of CO_2 per e^- (**Fig. 6c**). Molecular phenazine compounds have shown capacities closer to 1 equiv of CO_2 per e^-.[47–49] However, because our phenazine groups are highly substituted, we hypothesize that CO_2 is only able to bind to one of the two reduced nitrogen centers due to steric constraints (**Fig. 6a**). Quinone-based sorbents show similar steric sensitivity.[52,53] For example, the doubly reduced dianion of

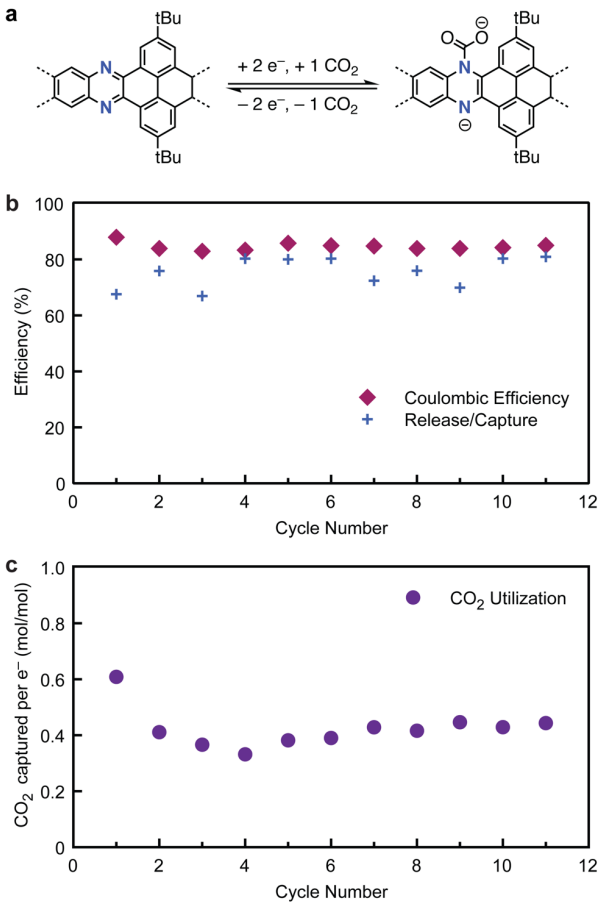

Fig. 6 | Overview of the (a) CO_2 capture mechanism, (b) Coulombic efficiency and release/capture efficiency, and (c) CO_2 capacity utilization for **2-tBuPyr**.

tetrachlorobenzoquinone is only able to capture one molecule of CO_2, rather than two, due to steric hindrance from the chloride substituents.[52] In addition to these steric arguments, it is also possible that the highly conjugated structure decreases the electron density on the nitrogen center, reducing the affinity of CO_2.

We next assessed the EMCC performance of **CS-COF**, the analogous phenazine-based 2D COF.[20] To our surprise, the CVs of the COF under N_2 and CO_2 atmospheres are nearly identical, suggesting the absence of CO_2 adduct formation (**Fig. S37**). Furthermore, the fixed-bed EMCC device shows no detectable CO_2 capture or release activity (**Fig. 5b**). Relative to the parent COF, we attribute the dramatic performance enhancement of our macrocycle nanoparticles to their greater colloidal stability and external surface area, which facilitates more intimate contact with the conductive additives, electrolyte, and CO_2. In particular, the improved electrical contact greatly increases the number of electrochemically accessible phenazine binding sites.

To quantify the number of electrochemically accessible phenazine sites in **2-tBuPyr**, discharge curves were performed. The capacity of **2-tBuPyr** electrodes was determined to be 33.35 mAh/g, indicating that approximately 23% of the phenazine sites per macrocycle could be accessed during the electrochemical process (see the SI for more details). While there is room for improvement, this unoptimized value is already much higher than those reported for several previously reported redox-active COFs. For example, Dichtel and coworkers showed that only ~3% of the redox-active groups in an anthraquinone-based COF were accessible when electrodes were fabricated from insoluble COF powders, due to poor electrical contact.[54] This value could be increased to 80–99% by carefully growing oriented thin films.[54] Similarly, Yaghi, Chang, and coworkers showed that only ~4–8% of the cobalt porphyrin centers in a 2D COF-based electrocatalyst were electroactive, due to limited electrochemical contact between the COF powder and the electrode.[55]

Together, these results establish phenazine-based macrocycles as competent solid sorbents for EMCC. We note that all prior work on EMCC with phenazine species and other sp^2-nitrogen containing molecules were studied in flow systems, using liquid sorbents.[47–49] This is the first demonstration of a non-quinone-based solid sorbent in a fixed-bed EMCC device.[56–58] At the same time, this work motivates further studies to improve the electrochemical accessibility of phenazine binding sites, identify structure–property relationships, and further improve the performance of this class of sorbents.

Conclusion. In summary, we have developed a new nitrogen-based ditopic ligand, H_4TNTP-OC4, which is compatible with diverse coordination chemistry and dynamic covalent chemistry reactions. Using this versatile building block, we have constructed three fully conjugated and shape-persistent macrocyclic cores with strong interlayer stacking, semiconducting behavior, and high chemical stability. Specifically, metalating our ditopic ligand with nickel(II) salts leads to fully conjugated nickel macrocycles with pressed pellet conductivities on the order of 10^{-3} S/cm. Similarly, the reaction of H_4TNTP-OC4·4HCl with tetraketones leads to a new family of organic macrocycles with robust phenazine linkages.

Our studies on electrochemically mediated CO_2 capture clearly illustrate the engineering benefits of macrocycles relative to bulk COF powders. The colloidal stability of our phenazine macrocycle nanoparticles facilitates intimate mixing with conductive additives and good electrical contact. As a result, phenazine macrocycles are competent sorbents for electrochemically mediated CO_2 capture, whereas phenazine COFs show negligible CO_2 uptake under the same conditions. Together, this work illustrates how simple macrocycles preserve key features of crystalline porous frameworks while providing distinct advantages in applications where processability and nanoscale dimensions are paramount.

ASSOCIATED CONTENT

Supporting Information

The Supporting Information is available free of charge on the ACS Publications website.

Additional experimental details, synthetic procedures, and characterization data (PDF)

AUTHOR INFORMATION

Corresponding Author

* Correspondence to: djxiao@uw.edu.

ACKNOWLEDGMENT

The work described here was primarily supported by the U.S. Department of Energy, Office of Science, Office of Basic Energy Sciences under Award Number DE-SC0021966. The synthesis of the phenazine macrocycles was additionally supported by the Arnold and Mabel Beckman Foundation through a Beckman Young Investigator Award. Additional characterization efforts were supported by the David and Lucile Packard Foundation. P.H.L. was supported in part by the state of Washington through graduate fellowships from the University of Washington Clean Energy Institute. J.G. and A.A.K. were supported by NSF graduate research fellowship. A.L. and Y.L. acknowledge financial support from the National Science Foundation (award number 237096). The authors acknowledge the use of instrumentation at the following shared facilities: the Washington Research Training Testbeds, a facility operated by the University of Washington Clean Energy Institute; the Molecular Analysis Facility, a National Nanotechnology Coordinated Infrastructure (NNCI) site at the University of Washington, which is supported in part by funds from the National Science Foundation (awards NNCI-2025489, NNCI-15421010), the Molecular Engineering & Sciences Institute, and the Clean Energy Institute; and the University of Washington Department of Chemistry. This research used resources of the Advanced Photon Source, a U.S. Department of Energy (DOE) Office of Science User Facility operated for the DOE Office of Science by Argonne National Laboratory under Contract No. DE-AC02-06CH11357. The mail-in program at Beamline 17-BM contributed to the data. Finally, we gratefully acknowledge Dr. Samantha Young for assistance in collecting and analyzing XPS data, Dr. Adrienne Roehrich for assistance in collecting and analyzing solid-state NMR data, and Rachel Tenney Smith for assistance in collecting and analyzing UV-Vis data.

REFERENCES

(1) Wang, S.; McGuirk, C. M.; d'Aquino, A.; Mason, J. A.; Mirkin, C. A. Metal–Organic Framework Nanoparticles. *Adv. Mater.* **2018**, *30* (37), 1800202. https://doi.org/10.1002/adma.201800202.

(2) Cai, X.; Xie, Z.; Li, D.; Kassymova, M.; Zang, S.-Q.; Jiang, H.-L. Nano-Sized Metal-Organic Frameworks: Synthesis and Applications. *Coordination Chemistry Reviews* **2020**, *417*, 213366. https://doi.org/10.1016/j.ccr.2020.213366.

(3) Ploetz, E.; Engelke, H.; Lächelt, U.; Wuttke, S. The Chemistry of Reticular Framework Nanoparticles: MOF, ZIF, and COF Materials. *Adv. Funct. Mater.* **2020**, *30* (41), 1909062. https://doi.org/10.1002/adfm.201909062.

(4) Cooper, A. I. Porous Molecular Solids and Liquids. *ACS Cent. Sci.* **2017**, *3* (6), 544–553. https://doi.org/10.1021/acscentsci.7b00146.

(5) Hosono, N.; Kitagawa, S. Modular Design of Porous Soft Materials via Self-Organization of Metal–Organic Cages. *Acc. Chem. Res.* **2018**, *51* (10), 2437–2446. https://doi.org/10.1021/acs.accounts.8b00361.

(6) Gosselin, A. J.; Rowland, C. A.; Bloch, E. D. Permanently Microporous Metal–Organic Polyhedra. *Chem. Rev.* **2020**, *120* (16), 8987–9014. https://doi.org/10.1021/acs.chemrev.9b00803.

(7) Strauss, M. J.; Evans, A. M.; Roesner, E. K.; Monsky, R. J.; Bardot, M. I.; Dichtel, W. R. Divergent Nanotube Synthesis through Reversible Macrocycle Assembly. *Acc. Mater. Res.* **2022**, *3* (9), 935–947. https://doi.org/10.1021/accountsmr.2c00062.

(8) Sánchez-González, E.; Tsang, M. Y.; Troyano, J.; Craig, G. A.; Furukawa, S. Assembling Metal–Organic Cages as Porous Materials. *Chem. Soc. Rev.* **2022**, *51* (12), 4876–4889. https://doi.org/10.1039/D1CS00759A.

(9) Pastore, V. J.; Cook, T. R. Coordination-Driven Self-Assembly in Polymer–Inorganic Hybrid Materials. *Chem. Mater.* **2020**, *32* (9), 3680–3700. https://doi.org/10.1021/acs.chemmater.0c00851.

(10) He, A.; Jiang, Z.; Wu, Y.; Hussain, H.; Rawle, J.; Briggs, M. E.; Little, M. A.; Livingston, A. G.; Cooper, A. I. A Smart and Responsive Crystalline Porous Organic Cage Membrane with Switchable Pore Apertures for Graded Molecular Sieving. *Nat. Mater.* **2022**, *21* (4), 463–470. https://doi.org/10.1038/s41563-021-01168-z.

(11) Jiang, Z.; Dong, R.; Evans, A. M.; Biere, N.; Ebrahim, M. A.; Li, S.; Anselmetti, D.; Dichtel, W. R.; Livingston, A. G. Aligned Macrocycle Pores in Ultrathin Films for Accurate Molecular Sieving. *Nature* **2022**, *609* (7925), 58–64. https://doi.org/10.1038/s41586-022-05032-1.

(12) Zasada, L. B.; Guio, L.; Kamin, A. A.; Dhakal, D.; Monahan, M.; Seidler, G. T.; Luscombe, C. K.; Xiao, D. J. Conjugated Metal–Organic Macrocycles: Synthesis, Characterization, and Electrical Conductivity. *J. Am. Chem. Soc.* **2022**, *144* (10), 4515–4521. https://doi.org/10.1021/jacs.1c12596.

(13) Smith, P. T.; Benke, B. P.; Cao, Z.; Kim, Y.; Nichols, E. M.; Kim, K.; Chang, C. J. Iron Porphyrins Embedded into a Supramolecular Porous Organic Cage for Electrochemical CO_2 Reduction in Water. *Angew Chem Int Ed* **2018**, *57* (31), 9684–9688. https://doi.org/10.1002/anie.201803873.

(14) Smith, P. T.; Kim, Y.; Benke, B. P.; Kim, K.; Chang, C. J. Supramolecular Tuning Enables Selective Oxygen Reduction Catalyzed by Cobalt Porphyrins for Direct Electrosynthesis of Hydrogen Peroxide. *Angew Chem Int Ed* **2020**, *59* (12), 4902–4907. https://doi.org/10.1002/anie.201916131.

(15) Gosselin, A. J.; Decker, G. E.; Antonio, A. M.; Lorzing, G. R.; Yap, G. P. A.; Bloch, E. D. A Charged Coordination Cage-Based Porous Salt. *J. Am. Chem. Soc.* **2020**, *142* (21), 9594–9598. https://doi.org/10.1021/jacs.0c02806.

(16) Jones, J. T. A.; Holden, D.; Mitra, T.; Hasell, T.; Adams, D. J.; Jelfs, K. E.; Trewin, A.; Willock, D. J.; Day, G. M.; Bacsa, J.; Steiner, A.; Cooper, A. I. On-Off Porosity Switching in a Molecular Organic Solid. *Angew. Chem. Int. Ed.* **2011**, *50* (3), 749–753. https://doi.org/10.1002/anie.201006030.

(17) Strauss, M. J.; Asheghali, D.; Evans, A. M.; Li, R. L.; Chavez, A. D.; Sun, C.; Becker, M. L.; Dichtel, W. R. Cooperative Self-Assembly of Pyridine-2,6-Diimine-Linked Macrocycles into Mechanically Robust Nanotubes. *Angew. Chem.* **2019**, *131* (41), 14850–14856. https://doi.org/10.1002/ange.201907668.

(18) Troyano, J.; Horike, S.; Furukawa, S. Reversible Discrete-to-Extended Metal–Organic Polyhedra Transformation by Sulfonic Acid Surface Functionalization. *J. Am. Chem. Soc.* **2022**, *144* (42), 19475–19484. https://doi.org/10.1021/jacs.2c07978.

(19) Zasada, L. B.; Le, P. H.; Hill, A. M.; Shafranek, R. T.; Xiao, D. J. Controlling the Crystal Packing and Morphology of Metal–Organic Macrocycles through Side-Chain Modification. *ACS Materials Lett.* **2024**, *6* (7), 3043–3049. https://doi.org/10.1021/acsmaterialslett.4c00957.

(20) Guo, J.; Xu, Y.; Jin, S.; Chen, L.; Kaji, T.; Honsho, Y.; Addicoat, M. A.; Kim, J.; Saeki, A.; Ihee, H.; Seki, S.; Irle, S.; Hiramoto, M.; Gao, J.; Jiang, D. Conjugated Organic Framework with Three-Dimensionally Ordered Stable Structure and Delocalized π Clouds. *Nat Commun* **2013**, *4* (1), 2736. https://doi.org/10.1038/ncomms3736.

(21) Mahmood, J.; Lee, E. K.; Jung, M.; Shin, D.; Jeon, I.-Y.; Jung, S.-M.; Choi, H.-J.; Seo, J.-M.; Bae, S.-Y.; Sohn, S.-D.; Park, N.; Oh, J. H.; Shin, H.-J.; Baek, J.-B. Nitrogenated Holey Two-Dimensional Structures. *Nat Commun* **2015**, *6* (1), 6486. https://doi.org/10.1038/ncomms7486.

(22) Meng, Z.; Stolz, R. M.; Mirica, K. A. Two-Dimensional Chemiresistive Covalent Organic Framework with High Intrinsic Conductivity. *J. Am. Chem. Soc.* **2019**, *141* (30), 11929–11937. https://doi.org/10.1021/jacs.9b03441.

(23) Wang, M.; Ballabio, M.; Wang, M.; Lin, H.-H.; Biswal, B. P.; Han, X.; Paasch, S.; Brunner, E.; Liu, P.; Chen, M.; Bonn, M.; Heine, T.; Zhou, S.; Cánovas, E.; Dong, R.; Feng, X. Unveiling Electronic Properties in Metal–Phthalocyanine-Based Pyrazine-Linked Conjugated Two-Dimensional Covalent Organic Frameworks. *J. Am. Chem. Soc.* **2019**, *141* (42), 16810–16816. https://doi.org/10.1021/jacs.9b07644.

(24) Li, X.; Wang, H.; Chen, H.; Zheng, Q.; Zhang, Q.; Mao, H.; Liu, Y.; Cai, S.; Sun, B.; Dun, C.; Gordon, M. P.; Zheng, H.; Reimer, J. A.; Urban, J. J.; Ciston, J.; Tan, T.; Chan, E. M.; Zhang, J.; Liu, Y. Dynamic Covalent Synthesis of Crystalline Porous Graphitic Frameworks. *Chem* **2020**, *6* (4), 933–944. https://doi.org/10.1016/j.chempr.2020.01.011.

(25) Das, P.; Mandal, S. K. In-Depth Experimental and Computational Investigations for Remarkable Gas/Vapor Sorption, Selectivity, and Affinity by a Porous Nitrogen-Rich Covalent Organic Framework. *Chem. Mater.* **2019**, *31* (5), 1584–1596. https://doi.org/10.1021/acs.chemmater.8b04683.

(26) Ranjeesh, K. C.; Illathvalappil, R.; Veer, S. D.; Peter, J.; Wakchaure, V. C.; Goudappagouda; Raj, K. V.; Kurungot, S.; Babu, S. S. Imidazole-Linked Crystalline Two-Dimensional Polymer with Ultrahigh Proton-Conductivity. *J. Am. Chem. Soc.* **2019**, *141* (38), 14950–14954. https://doi.org/10.1021/jacs.9b06080.

(27) Zhou, R.; Huang, Y.; Li, Z.; Kang, S.; Wang, X.; Liu, S. Piperazine-Based Two-Dimensional Covalent Organic Framework for High Performance Anodic Lithium Storage. *Energy Storage Materials* **2021**, *40*, 124–138. https://doi.org/10.1016/j.ensm.2021.05.008.

(28) Yue, Y.; Li, H.; Chen, H.; Huang, N. Piperazine-Linked Covalent Organic Frameworks with High Electrical Conductivity. *J. Am. Chem. Soc.* **2022**, *144* (7), 2873–2878. https://doi.org/10.1021/jacs.1c13012.

(29) Xie, L. S.; Skorupskii, G.; Dincă, M. Electrically Conductive Metal–Organic Frameworks. *Chem. Rev.* **2020**, *120* (16), 8536–8580. https://doi.org/10.1021/acs.chemrev.9b00766.

(30) Sheberla, D.; Sun, L.; Blood-Forsythe, M. A.; Er, S.; Wade, C. R.; Brozek, C. K.; Aspuru-Guzik, A.; Dincă, M. High Electrical Conductivity in Ni3(2,3,6,7,10,11-Hexaiminotriphenylene)2, a Semiconducting Metal–Organic Graphene Analogue. *J. Am. Chem. Soc.* **2014**, *136* (25), 8859–8862. https://doi.org/10.1021/ja502765n.

(31) Smith, M. K.; Powers-Riggs, N. E.; Northrop, B. H. Rational Synthesis of Bis(Hexyloxy)-Tetra(Hydroxy)-Triphenylenes and Their Derivatives. *RSC Adv.* **2014**, *4* (72), 38281–38292. https://doi.org/10.1039/C4RA06503D.

(32) Chen, T.; Dou, J.-H.; Yang, L.; Sun, C.; Libretto, N. J.; Skorupskii, G.; Miller, J. T.; Dincă, M. Continuous Electrical Conductivity Variation in M_3 (Hexaiminotriphenylene)$_2$ (M = Co, Ni, Cu) MOF Alloys. *J. Am. Chem. Soc.* **2020**, *142* (28), 12367–12373. https://doi.org/10.1021/jacs.0c04458.

(33) Day, R. W.; Bediako, D. K.; Rezaee, M.; Parent, L. R.; Skorupskii, G.; Arguilla, M. Q.; Hendon, C. H.; Stassen, I.; Gianneschi, N. C.; Kim, P.; Dincă, M. Single Crystals of Electrically Conductive Two-Dimensional Metal–Organic Frameworks: Structural and Electrical Transport Properties. *ACS Cent. Sci.* **2019**, *5* (12), 1959–1964. https://doi.org/10.1021/acscentsci.9b01006.

(34) Dou, J.-H.; Arguilla, M. Q.; Luo, Y.; Li, J.; Zhang, W.; Sun, L.; Mancuso, J. L.; Yang, L.; Chen, T.; Parent, L. R.; Skorupskii, G.; Libretto, N. J.; Sun, C.; Yang, M. C.; Dip, P. V.; Brignole, E. J.; Miller, J. T.; Kong, J.; Hendon, C. H.; Sun, J.; Dincă, M. Atomically Precise Single-Crystal Structures of Electrically Conducting 2D Metal–Organic Frameworks. *Nature Materials* **2021**, *20* (2), 222–228. https://doi.org/10.1038/s41563-020-00847-7.

(35) Matienzo, J.; Yin, L. I.; Grim, S. O.; Swartz, W. E. X-Ray Photoelectron Spectroscopy of Nickel Compounds. *Inorg. Chem.* **1973**, *12* (12), 2762–2769. https://doi.org/10.1021/ic50130a005.

(36) Stolz, R. M.; Mahdavi-Shakib, A.; Frederick, B. G.; Mirica, K. A. Host–Guest Interactions and Redox Activity in Layered Conductive Metal–Organic Frameworks. *Chem. Mater.* **2020**, *32* (18), 7639–7652. https://doi.org/10.1021/acs.chemmater.0c01007.

(37) Artyushkova, K. Misconceptions in Interpretation of Nitrogen Chemistry from X-Ray Photoelectron Spectra. *Journal of Vacuum Science & Technology A: Vacuum, Surfaces, and Films* **2020**, *38* (3), 031002. https://doi.org/10.1116/1.5135923.

(38) Chavez, A. D.; Smith, B. J.; Smith, M. K.; Beaucage, P. A.; Northrop, B. H.; Dichtel, W. R. Discrete, Hexagonal Boronate Ester-Linked Macrocycles Related to Two-Dimensional Covalent Organic Frameworks. *Chem. Mater.* **2016**, *28* (14), 4884–4888. https://doi.org/10.1021/acs.chemmater.6b01831.

(39) Sheberla, D.; Sun, L.; Blood-Forsythe, M. A.; Er, S.; Wade, C. R.; Brozek, C. K.; Aspuru-Guzik, A.; Dincă, M. High Electrical Conductivity in Ni_3 (2,3,6,7,10,11-Hexaiminotriphenylene)$_2$, a Semiconducting Metal–Organic Graphene Analogue. *J. Am. Chem. Soc.* **2014**, *136* (25), 8859–8862. https://doi.org/10.1021/ja502765n.

(40) Wu, X.; Han, X.; Liu, Y.; Liu, Y.; Cui, Y. Control Interlayer Stacking and Chemical Stability of Two-Dimensional Covalent Organic Frameworks via Steric Tuning. *J. Am. Chem. Soc.* **2018**, *140* (47), 16124–16133. https://doi.org/10.1021/jacs.8b08452.

(41) Kang, C.; Zhang, Z.; Wee, V.; Usadi, A. K.; Calabro, D. C.; Baugh, L. S.; Wang, S.; Wang, Y.; Zhao, D. Interlayer Shifting in Two-Dimensional Covalent Organic Frameworks. *J. Am. Chem. Soc.* **2020**, *142* (30), 12995–13002. https://doi.org/10.1021/jacs.0c03691.

(42) Bian, G.; Yin, J.; Zhu, J. Recent Advances on Conductive 2D Covalent Organic Frameworks. *Small* **2021**, *17* (22), 2006043. https://doi.org/10.1002/smll.202006043.

(43) Yang, Y.; Börjesson, K. Electroactive Covalent Organic Frameworks: A New Choice for Organic Electronics. *Trends in Chemistry* **2022**, *4* (1), 60–75. https://doi.org/10.1016/j.trechm.2021.10.007.

(44) Smith, B. J.; Parent, L. R.; Overholts, A. C.; Beaucage, P. A.; Bisbey, R. P.; Chavez, A. D.; Hwang, N.; Park, C.; Evans, A. M.; Gianneschi, N. C.; Dichtel, W. R. Colloidal Covalent Organic Frameworks. *ACS Cent. Sci.* **2017**, *3* (1), 58–65. https://doi.org/10.1021/acscentsci.6b00331.

(45) Zhao, Y.; Guo, L.; Gándara, F.; Ma, Y.; Liu, Z.; Zhu, C.; Lyu, H.; Trickett, C. A.; Kapustin, E. A.; Terasaki, O.; Yaghi, O. M. A Synthetic Route for Crystals of Woven Structures, Uniform Nanocrystals, and Thin Films of Imine Covalent Organic Frameworks. *J. Am. Chem. Soc.* **2017**, *139* (37), 13166–13172. https://doi.org/10.1021/jacs.7b07457.

(46) Khalil, S.; Meyer, M. D.; Alazmi, A.; Samani, M. H. K.; Huang, P.-C.; Barnes, M.; Marciel, A. B.; Verduzco, R. Enabling Solution Processable COFs through Suppression of Precipitation during Solvothermal Synthesis. *ACS Nano* **2022**, *16* (12), 20964–20974. https://doi.org/10.1021/acsnano.2c08580.

(47) Li, X.; Zhao, X.; Liu, Y.; Hatton, T. A.; Liu, Y. Redox-Tunable Lewis Bases for Electrochemical Carbon Dioxide Capture. *Nat Energy* **2022**, *7* (11), 1065–1075. https://doi.org/10.1038/s41560-022-01137-z.

(48) Seo, H.; Hatton, T. A. Electrochemical Direct Air Capture of CO2 Using Neutral Red as Reversible Redox-Active Material. *Nat Commun* **2023**, *14* (1), 313. https://doi.org/10.1038/s41467-023-35866-w.

(49) Pang, S.; Jin, S.; Yang, F.; Alberts, M.; Li, L.; Xi, D.; Gordon, R. G.; Wang, P.; Aziz, M. J.; Ji, Y. A Phenazine-Based High-Capacity and High-Stability Electrochemical CO2 Capture Cell with Coupled Electricity Storage. *Nat Energy* **2023**, *8* (10), 1126–1136. https://doi.org/10.1038/s41560-023-01347-z.

(50) Li, X.; Mathur, A.; Liu, A.; Liu, Y. Electrifying Carbon Capture by Developing Nanomaterials at the Interface of Molecular and Process Engineering. *Acc. Chem. Res.* **2023**, *56* (20), 2763–2775. https://doi.org/10.1021/acs.accounts.3c00321.

(51) Jayarapu, K. N.; Mathur, A.; Li, X.; Liu, A.; Zhang, L.; Kim, J.; Kim, H.; Kuk, S. K.; Liu, Y. Indigo as a Low-Cost Redox-Active Sorbent for Electrochemically Mediated Carbon Capture. *Advanced Functional Materials n/a* (n/a), 2402355. https://doi.org/10.1002/adfm.202402355.

(52) Nagaoka, T.; Nishii, N.; Fujii, K.; Ogura, K. Mechanisms of Reductive Addition of CO2 to Quinones in Acetonitrile. *Journal of Electroanalytical Chemistry* **1992**, *322* (1–2), 383–389. https://doi.org/10.1016/0022-0728(92)80090-Q.

(53) Bui, A. T.; Hartley, N. A.; Thom, A. J. W.; Forse, A. C. Trade-Off between Redox Potential and the Strength of Electrochemical CO_2 Capture in Quinones. *J. Phys. Chem. C* **2022**, *126* (33), 14163–14172. https://doi.org/10.1021/acs.jpcc.2c03752.

(54) DeBlase, C. R.; Hernández-Burgos, K.; Silberstein, K. E.; Rodríguez-Calero, G. G.; Bisbey, R. P.; Abruña, H. D.; Dichtel, W. R. Rapid and Efficient Redox Processes within 2D Covalent Organic Framework Thin Films. *ACS Nano* **2015**, *9* (3), 3178–3183. https://doi.org/10.1021/acsnano.5b00184.

(55) Lin, S.; Diercks, C. S.; Zhang, Y.-B.; Kornienko, N.; Nichols, E. M.; Zhao, Y.; Paris, A. R.; Kim, D.; Yang, P.; Yaghi, O. M.; Chang, C. J. Covalent Organic Frameworks

Comprising Cobalt Porphyrins for Catalytic CO_2 Reduction in Water. *Science* **2015**, *349* (6253), 1208–1213. https://doi.org/10.1126/science.aac8343.

(56) Voskian, S.; Hatton, T. A. Faradaic Electro-Swing Reactive Adsorption for CO_2 Capture. *Energy Environ. Sci.* **2019**, *12* (12), 3530–3547. https://doi.org/10.1039/C9EE02412C.

(57) Liu, Y.; Ye, H.-Z.; Diederichsen, K. M.; Van Voorhis, T.; Hatton, T. A. Electrochemically Mediated Carbon Dioxide Separation with Quinone Chemistry in Salt-Concentrated Aqueous Media. *Nat Commun* **2020**, *11* (1), 2278. https://doi.org/10.1038/s41467-020-16150-7.

(58) Hemmatifar, A.; Kang, J. S.; Ozbek, N.; Tan, K.; Hatton, T. A. Electrochemically Mediated Direct CO_2 Capture by a Stackable Bipolar Cell. *ChemSusChem* **2022**, *15* (6), e202102533. https://doi.org/10.1002/cssc.202102533.